

Article

# Effects of Post Heat Treatments on Microstructures and Mechanical Properties of Selective Laser Melted Ti6Al4V Alloy

Jianwen Liu <sup>1</sup>, Jie Liu <sup>1</sup>, Yixin Li <sup>1</sup>, Ruifeng Zhang <sup>2</sup>, Zhuoran Zeng <sup>3</sup>, Yuman Zhu <sup>4</sup> , Kai Zhang <sup>1,4,\*</sup> and Aijun Huang <sup>4</sup>

<sup>1</sup> School of Material Science and Engineering, University of Shanghai for Science and Technology, Shanghai 200093, China; asap.liu@hotmail.com (J.L.); liujie1998221@hotmail.com (J.L.); xiaonibalyx@163.com (Y.L.)

<sup>2</sup> School of Materials Science and Engineering, Central South University, Changsha 410083, China; ruifeng.zhang@csu.edu.cn

<sup>3</sup> College of Engineering and Computer Science, Australian National University, Acton, ACT 2601, Australia; zhuoran.zeng@anu.edu.au

<sup>4</sup> Monash Center for Additive Manufacturing (MCAM), Monash University, Notting Hill, VIC 3168, Australia; yuman.zhu@monash.edu (Y.Z.); aijun.huang@monash.edu (A.H.)

\* Correspondence: kai.zhang@usst.edu.cn; Tel.: +86-021-55270108

**Abstract:** The unique thermal history of selective laser melting (SLM) can lead to high residual stress and a non-equilibrium state in as-fabricated titanium alloy components and hinders their extensive use. Post heat treatment, as a classical and effective way, could transform non-equilibrium  $\alpha'$  martensite and achieves desirable mechanical performance in SLMed Ti alloys. In this study, we aimed to establish the correlation between the microstructure and mechanical performances of SLMed Ti6Al4V (Ti-64) by using different heat treatment processes. The columnar prior  $\beta$  grain morphology and grain boundary  $\alpha$  phase (GB- $\alpha$ ) after different heat treatment processes were characterized, with their influences on the tensile property anisotropy fully investigated. Scanning electron microscope (SEM) observation of the fracture surface and its cross-sectional analysis found that the tensile properties, especially the ductility, were affected by the GB- $\alpha$  along the  $\beta$  grain boundary. Furthermore, the discontinuous ratio of GB- $\alpha$  was firstly proposed to quantitatively predict the anisotropic ductility in SLMed Ti-64. This study provides a step forward for achieving the mechanical property manipulation of SLMed Ti-64 parts.

**Keywords:** selective laser melting; Ti-6Al-4V;  $\alpha$  lath; grain boundary  $\alpha$  phase; tensile performance



**Citation:** Liu, J.; Liu, J.; Li, Y.; Zhang, R.; Zeng, Z.; Zhu, Y.; Zhang, K.; Huang, A. Effects of Post Heat Treatments on Microstructures and Mechanical Properties of Selective Laser Melted Ti6Al4V Alloy. *Metals* **2021**, *11*, 1593. <https://doi.org/10.3390/met11101593>

Academic Editor: Thomas Niendorf

Received: 29 August 2021

Accepted: 3 October 2021

Published: 7 October 2021

**Publisher's Note:** MDPI stays neutral with regard to jurisdictional claims in published maps and institutional affiliations.



**Copyright:** © 2021 by the authors. Licensee MDPI, Basel, Switzerland. This article is an open access article distributed under the terms and conditions of the Creative Commons Attribution (CC BY) license (<https://creativecommons.org/licenses/by/4.0/>).

## 1. Introduction

Additive manufacturing (AM), as opposed to the traditional subtractive manufacturing techniques, could build a three-dimensional component layer-by-layer with digital files [1–3]. AM has been demonstrated and adopted by aerospace, energy, and automotive industries for the benefits of more design freedom, low cost, and short prototyping time [2,4,5]. Compared to Direct Energy Deposition (DED), selective laser melting (SLM), which is laser-based powder bed fusion [6], is more suitable to fabricate small-scale components with complex geometries and high precision [7]. A wide variety of alloys have been utilized in SLM, ranging from superalloy [8,9], steel alloys [10,11], aluminum alloys [12,13], and titanium alloys [14,15]. Ti-6Al-4V (Ti-64) is the most extensively used titanium alloy due to its high specific strength, excellent corrosion resistance, and good mechanical performance [16].

However, the rapid solidification and the strong directional cooling along the build direction of the SLM process could lead to a non-equilibrium martensitic phase and large columnar  $\beta$  grains in as-fabricated titanium alloy [3,17]. Large columnar  $\beta$  grains along the build direction of the as-fabricated titanium alloys could lead to strong mechanical property

anisotropy, which makes the component design and product certification difficult [18,19]. It was reported that the trace element additions (like boron) to Ti alloys can effectively refine the prior  $\beta$  grain sizes because the trace element could provide additional grain nucleation sites and restrict grain growth during the solidification [20–23].

Post heat treatment, as a classical and effective way, could de-composite non-equilibrium  $\alpha'$  martensite and achieves desirable mechanical performances in SLMed titanium alloys [24,25]. The mechanical performance manipulation of SLMed Ti alloys is strongly governed by the microstructure features after heat treatments [26,27]. For instance, a decomposition of  $\alpha'$  martensite to the coarser  $\alpha$  lath during the annealing process could lead to the increase of ductility of SLMed Ti-6Al-4V [25]. With the increase of the thickness of  $\alpha$  lath, the tensile strength could decrease, with the correlation of  $\alpha$  lath thickness and tensile strength following the Hall–Petch relationship [28]. Furthermore, the presence of continuous grain boundary  $\alpha$  phase (GB- $\alpha$ ) in AMed Ti alloys could significantly reduce the fatigue performance and is also attributed to the ductility anisotropy [22]. Continuous GB- $\alpha$  along the fabrication direction could provide preferred crack pathways and lead to rapid fatigue failure through intergranular fracture [29,30]. In contrast, discontinuous GB- $\alpha$  could lead to transcrystalline fracture, which was attributed to the fine hardening secondary  $\alpha$  phase ( $\alpha_s$ ) between the discontinuous GB- $\alpha$  that could inhibit the crack propagation [31]. The microstructure feature like  $\alpha$  lath and their correlation with the mechanical properties is established, while the full correlation between GB- $\alpha$  characteristics and mechanical properties is not fully investigated.

In this study, we investigated the effects of heat treatment on the microstructure and tensile performances of SLMed Ti-6Al-4V along with the vertical and horizontal directions. Nine different combinations of annealing temperature (750, 850, and 950 °C) and cooling rate (water quenching, air cooling, furnace cooling) were selected for investigating the evolutions of prior  $\beta$  grain morphology and the  $\alpha$  phase. The tensile performances of the heat-treated SLMed Ti-64 were tested. Characterization of the fracture surface clarified the effect of microstructure on the failure mode. The strong ductility anisotropy was attributed to the prior  $\beta$  grain morphology. Providing that the prior  $\beta$  grain boundaries were decorated with the discontinuous GB- $\alpha$ , the transgranular fracture will occur, which reduced the ductility anisotropy. The correlation between the GB- $\alpha$  morphologies and tensile anisotropy was established in this study. This work proposed a simple approach for eliminating the anisotropy ductility and provided useful guidance for the design of the heat treatment process for SLMed titanium alloys.

## 2. Materials and Methods

Gas atomized pre-alloyed Ti-64 powder was manufactured by Falcon Tech Co., Ltd. in China. The powder sizes have a spherical morphology with particle sizes of 20.5 (D10), 35.0 (D50), and 55.2  $\mu\text{m}$  (D90) (Figure 1a). All SLMed Ti-64 samples were fabricated by EOS M290 machine. The processing parameters were laser power 265 W, scan speed 1100 mm/min, hatch distance 0.15 mm, and layer thickness 0.04 mm. The processing parameters were optimized by using Doehlert matrix method, specific details of the procedure can be found in [32,33]. The chemical compositions of SLMed Ti-64 are listed in Table 1. The relative density of the as-fabricated sample was measured at 99.9% by image analysis of 20 optical micrographs. The heat treatment process of SLMed Ti-64 samples ( $10 \times 10 \times 6 \text{ mm}^3$ ) was carried out in a tubular furnace (GSL-1200X). The post-heat treatment parameters are listed in Table 2.

For microstructural characterization, SLMed Ti-64 samples were ground with 220# to 5000# SiC papers, mechanically polished with a mixture of 10 vol%  $\text{H}_2\text{O}_2$  and 90 vol% Oxide Polishing Suspension (OP-S), and then etched with Kroll's reagent (95%  $\text{H}_2\text{O}$ , 4%  $\text{HNO}_3$ , and 1% HF). Optical microscopy (OM) images were obtained by Zeiss Imager M2m optical microscope. Field emission gun-scanning electron microscope (FEG-SEM, Zeiss Gemini SEM 300) was used to obtain secondary electron images and back-scattered electron images of SLMed Ti-64 with the working voltage 20 kV, probe current 15 nA and

work distance 5 mm. The detailed microstructure characterization of SLMed Ti-64 was carried out by using the open-source software ImageJ (10 OM images analyzed for each sample). The tensile samples were in two directions, including horizontal direction (HD) and vertical direction (VD) (Figure 1c), with the geometry of cylindrical tensile testing bars shown in Figure 1b. The tensile testing was carried out in a Zwick 100KN machine with a crosshead displacement rate of 0.6 mm/min. Two tensile samples were used to test the tensile performances of SLMed Ti-64 in each direction with consistent results obtained.

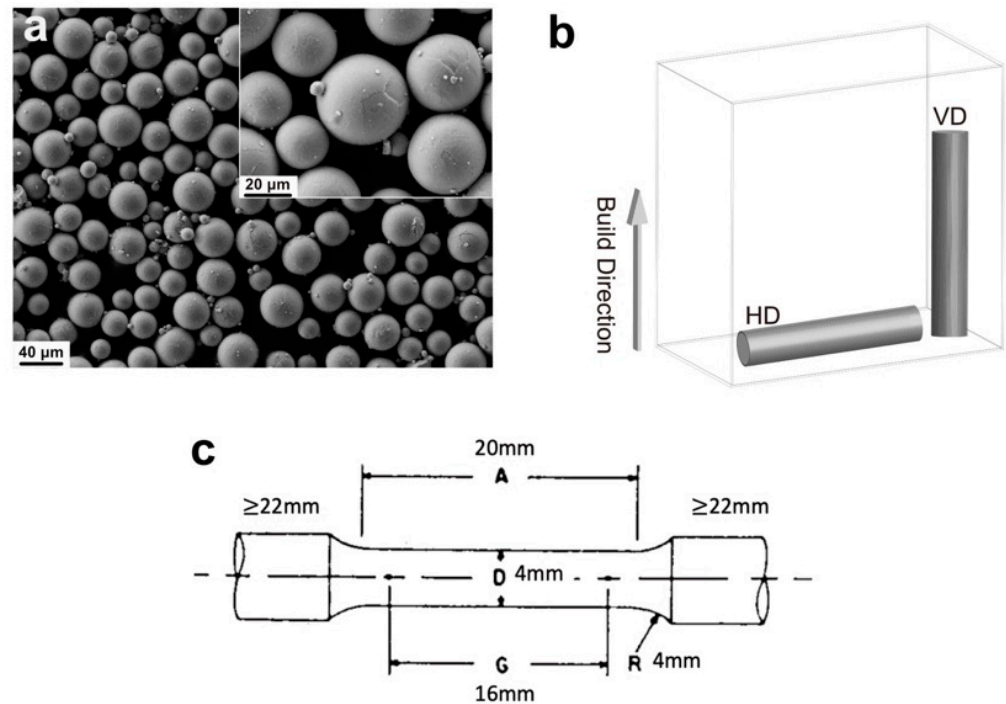


**Figure 1.** (a) SEM images of the Ti-64 powders used in this study. (b) Schematic of SLMed Ti-64 tensile samples; (c) schematic of the build directions of tensile specimens.

**Table 1.** Chemical composition of Ti-64.

Alloy (wt.%)	Al	V	O	Fe	C	N	H	Ti
Powder	6.18	3.94	0.0951	0.01	0.01	0.0133	0.0017	Bal.
As-fabricated	6.02	4.04	0.15	0.20	0.01	0.028	0.0043	Bal.

**Table 2.** Details of post-heat treatments.

ID	HT Temperature	Dwell Time	Cooling Mode
750-WQ	750 °C	2 h	Water quenching
750-AC			Air cooling
750-FC			Furnace cooling
850-WQ	850 °C	2 h	Water quenching
850-AC			Air cooling
850-FC			Furnace cooling
950-WQ	950 °C	2 h	Water quenching
950-AC			Air cooling
950-FC			Furnace cooling

### 3. Results

#### 3.1. Tensile Properties

Figure 2 shows the tensile performances for SLMed Ti-64 after different heat treatments (HT) along with two directions. For the WQ samples, the ultimate tensile stress

(UTS) and the yield stress (YS) increased with the increase of HT temperature, while the elongation (EL) decreased (Figure 2a). It was found that the 850-WQ sample has a good combination of strength and ductility, the UTS, YS, and EL in the horizontal direction were  $1012.5 \pm 20.1$  MPa,  $871.4 \pm 29.5$  MPa, and  $16.8 \pm 0.2\%$ , respectively. In comparison, the UTS, YS, and EL in the vertical sample were  $1057.2 \pm 0.3$  MPa,  $863.5 \pm 0.5$  MPa, and  $17.3 \pm 0.2\%$ , respectively. For the AC samples, with the HT temperature increasing, the UTS and YS decreased, while the EL increased slightly (Figure 2b). This shows the opposite trend as compared with that in WQ samples. The 850-AC sample in the vertical direction shows a trade-off between the strength and ductility, the UTS, YS, and EL were  $1022.6 \pm 1.0$  MPa,  $940.3 \pm 3.0$  MPa, and  $18.6 \pm 0.1\%$ , respectively. For the total elongation, there is a quite difference between the vertical direction ( $18.6 \pm 0.1\%$ ) and horizontal direction ( $14.2 \pm 0.4\%$ ) directions, which highlight the anisotropy in the ductility. For the FC samples, the UTS and YS decreased significantly with increasing the HT temperature, and their EL change little in three HT temperatures (Figure 2c). The UTS, YS, and EL of 750-FC samples in vertical direction were  $1044.1 \pm 1.0$  MPa,  $998.5 \pm 3.0$  MPa, and  $17.8 \pm 0.7\%$ , while those of 750-FC sample in the horizontal direction were  $1045.0 \pm 1.0$  MPa,  $970.4 \pm 10.0$  MPa, and  $14.4 \pm 0.2\%$ . Furthermore, for the tensile strength, there is a significant difference in the 850-FC sample, with the yield stress was  $890.0 \pm 9.0$  MPa in the horizontal direction and  $980.5 \pm 12.5$  MPa in the vertical direction.

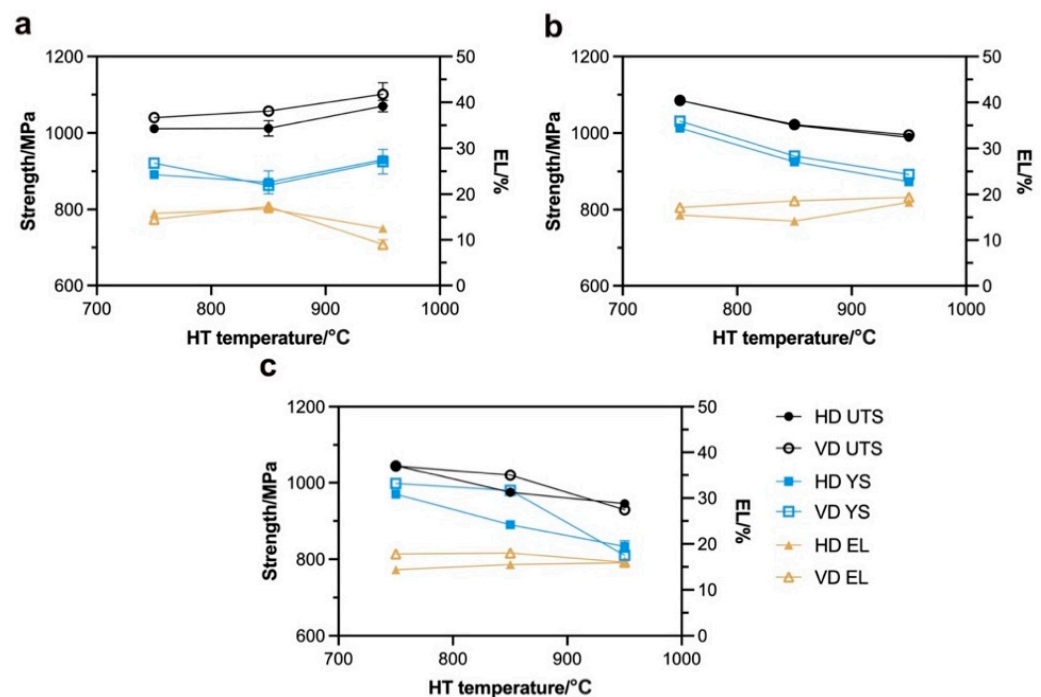


**Figure 2.** Tensile performances of SLMed Ti-64 after different heat treatment methods: (a) WQ samples, (b) AC samples, (c) FC samples. UTS: ultimate tensile strength, YS; yield strength, EL: elongation.

### 3.2. Microstructure Characterization

To understand the underlying mechanisms for the tensile property variations, we characterized the prior  $\beta$ -phase grain and  $\alpha$ -grain microstructure. The longitudinal direction of as-fabricated Ti-64 was composed of columnar prior  $\beta$  grains with an average width of  $139.20 \pm 38.58$   $\mu\text{m}$ , which was close to the hatch distance used for the sample fabrication (Figure 3). The columnar prior  $\beta$  grains were elongated along the fabrication direction, which was determined by the maximum thermal temperature gradient in the SLM deposition process, with an aspect ratio of approximately 7.2 [24,34]. The microstructure consisted of a fully acicular  $\alpha'$  martensitic microstructure with the average thickness measured as  $0.46 \pm 0.07$   $\mu\text{m}$ . Furthermore, we noticed that the GB- $\alpha$  is absent in an as-fabricated state,

which was attributed to the high cooling rate of the SLM process that inhibits the formation of GB- $\alpha$  [35].

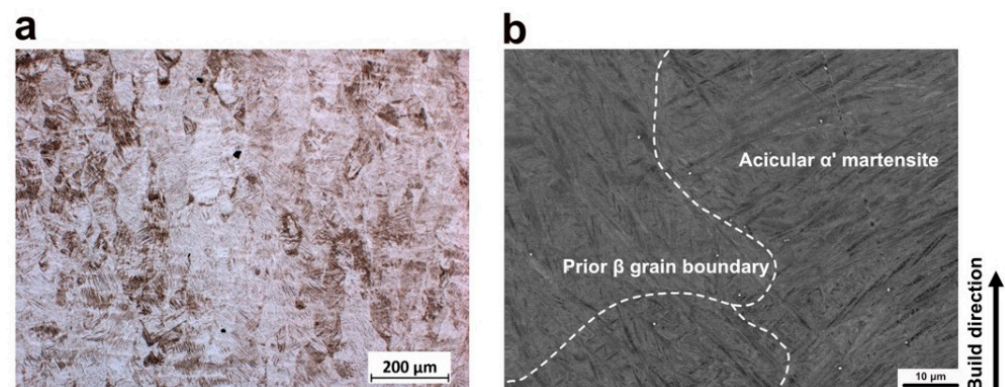


**Figure 3.** Microstructure of as-fabricated Ti-64 samples, (a) optical microscopy image; (b) back-scattered electron image.

### 3.2.1. Prior $\beta$ Microstructure Characterization with Different Heat Treatment

The width of prior  $\beta$  grains ranged from 30 to 350  $\mu\text{m}$ , with an average width of  $158.2 \pm 67.3 \mu\text{m}$  in 750-WQ sample,  $148.6 \pm 55.1 \mu\text{m}$  in 750-AC sample,  $178.6 \pm 64.6 \mu\text{m}$  in 750-FC sample, respectively (Figure 4a,c,e). These samples annealed at 750  $^{\circ}\text{C}$  have the prior  $\beta$  grain width close to the as-fabricated state. In addition, columnar prior  $\beta$  grains were elongated in the building direction, with the measured average aspect ratio approximately 5.4 in 750-WQ sample, 5.6 in 750-AC sample, and 6.4 in 750-FC sample (Figure 4a,c,e). The aspect ratio of prior  $\beta$  grains gradually increases with the cooling rate increases. After annealing at 750  $^{\circ}\text{C}$  for 2 h, the decomposition of non-equilibrium  $\alpha'$  martensite into a mixture of  $\alpha$  and  $\beta$  phases could be noticed. However, some prior  $\beta$  grains still consisted of the fine  $\alpha'$  martensite, suggesting that annealing at 750  $^{\circ}\text{C}$  for 2 h was insufficient to completely decompose the  $\alpha'$  martensite (yellow arrow in Figure 4). These retained  $\alpha'$  martensite could contribute to the high tensile strength [36].

The average width of prior  $\beta$  grains was  $161.0 \pm 44.9 \mu\text{m}$  in the 850-WQ sample,  $152.1 \pm 57.2 \mu\text{m}$  in the 850-AC sample,  $179.1 \pm 53.1 \mu\text{m}$  in the 850-FC sample, respectively (Figure 5). By comparing the measured results of the prior  $\beta$  grains in samples treated with different temperatures, it could be found that increasing the annealing treatment temperature could result in more  $\beta$  grain growth. In addition, the change of the cooling rates could vary the average aspect ratio of these  $\beta$  grains slightly: approximately 5.3 in the 850-WQ sample, 4.5 in the 850-AC sample, and 5.1 in the 850-FC sample. Furthermore, after annealing at 850  $^{\circ}\text{C}$  for 2 h, the fine  $\alpha$  phase was present inside the prior  $\beta$  grains, and  $\alpha'$  martensite was not observed. It shows that non-equilibrium  $\alpha'$  martensite decomposition into  $\alpha$  and  $\beta$  phases were mostly complete after 2 h at 850  $^{\circ}\text{C}$  in our study, which contributed to the good ductility of SLMed Ti-64 at 850  $^{\circ}\text{C}$  for 2 h.

The width of the prior  $\beta$  grains was measured as  $179.4 \pm 51.9 \mu\text{m}$  in the 950-WQ sample,  $172.1 \pm 51.6 \mu\text{m}$  in the 950-AC sample,  $203.4 \pm 60.1 \mu\text{m}$  in the 950-FC sample (Figure 6). The aspect ratios of the prior  $\beta$  grains were measured as approximately 3.7 in the 950-WQ sample, 2.9 in the 950-AC sample, and 3.1 in the 950-FC sample. Additionally, microstructural analysis shows that  $\alpha$  and  $\beta$  phases could be identified within the prior  $\beta$  grains in the samples with the air cooling or furnace cooling, whereas  $\alpha'$  martensite was found in the samples with water quenching. The presence of the  $\beta$  phase could be further identified by high-magnification SEM images (discuss in Section 3.2.2). In the samples treated at 950  $^{\circ}\text{C}$ , the equilibrium  $\alpha$ -fraction was reduced to approximately 23% [37]. More specifically, most  $\alpha$  phases in Figure 6 were re-transformed from the high-temperature  $\beta$  phase, instead of from the  $\alpha'$  (martensite structure)  $\rightarrow \alpha + \beta$  phase decomposition. Meanwhile, higher cooling rates, which could be introduced by using water quenching, could result in the  $\beta$  phase transforming to non-equilibrium  $\alpha'$  martensite phases [35]. The

hard and brittle acicular  $\alpha'$  martensite phase could result in the higher tensile strength and lower ductility, which explains why the tensile strength in WQ samples shows the opposite trend to AC/FC samples. More specifically, the tensile strength in WQ samples increased with HT temperature rising while tensile strength in AC/FC samples decreases obviously with the increase of temperature.

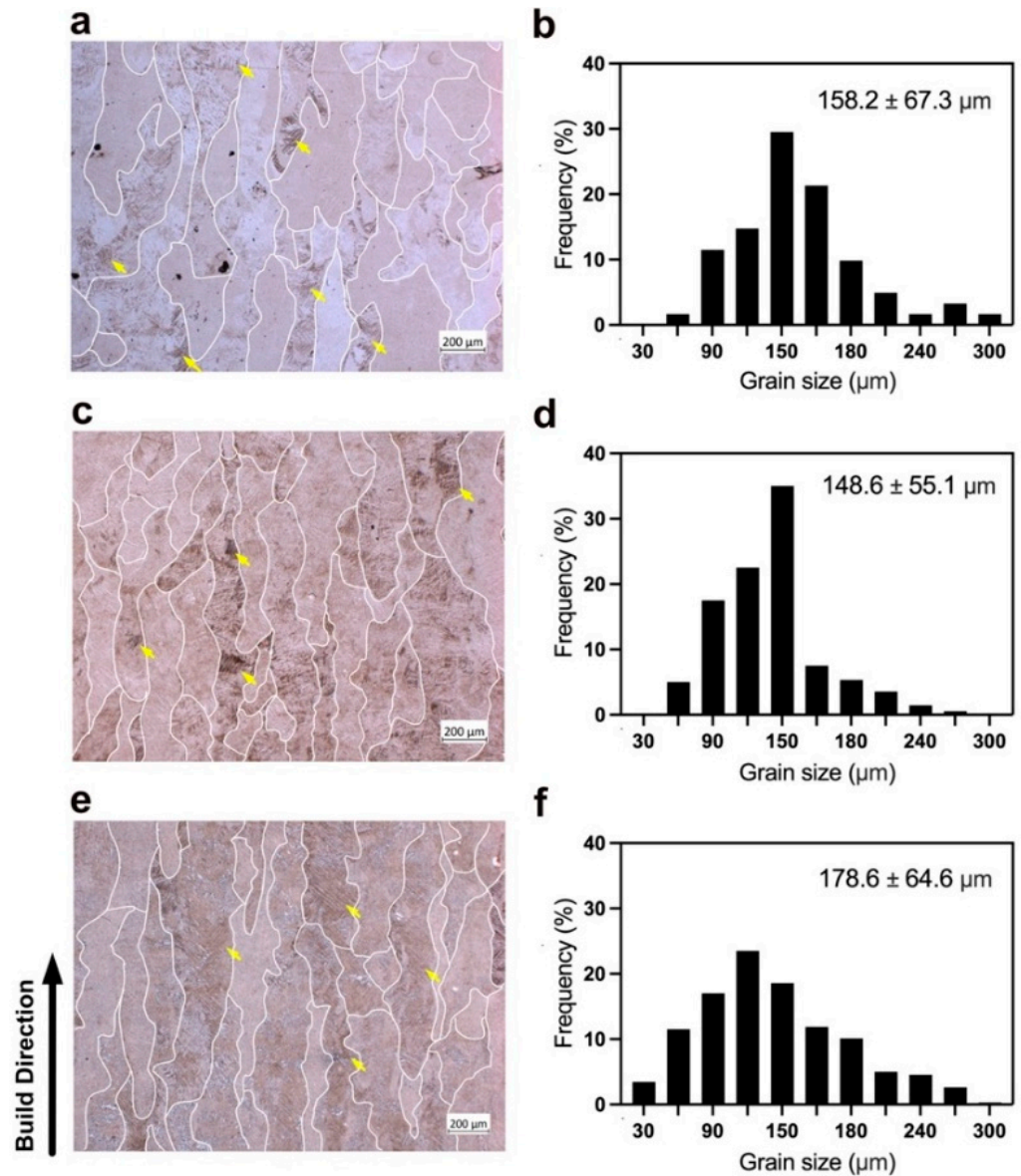


**Figure 4.** Representative optical microscopy images of (a) 750-WQ sample, (c) 750-AC sample, (e) 750-FC sample. The prior  $\beta$  grain boundaries in (a,c,e) are traced by white-color lines. The histograms of prior  $\beta$ -phase grains size are shown in (b,d,f).

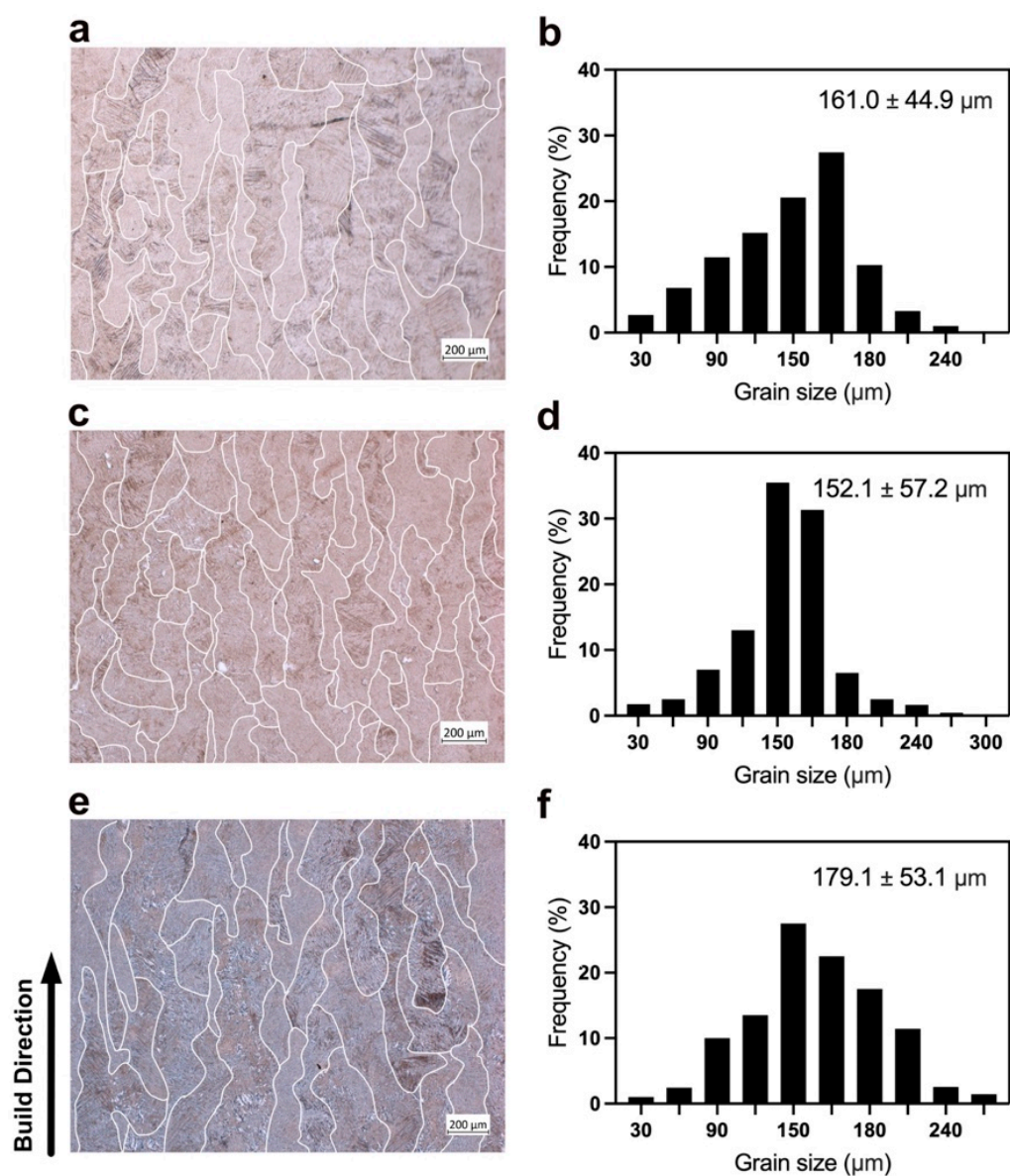


**Figure 5.** Representative optical microscopy images of (a) 850-WQ sample; (c) 850-AC sample; (e) 850-FC sample. The prior  $\beta$  grain boundaries in (a,c,e) are traced by white-color lines. The histograms of prior  $\beta$ -phase grains size are shown in (b,d,f).

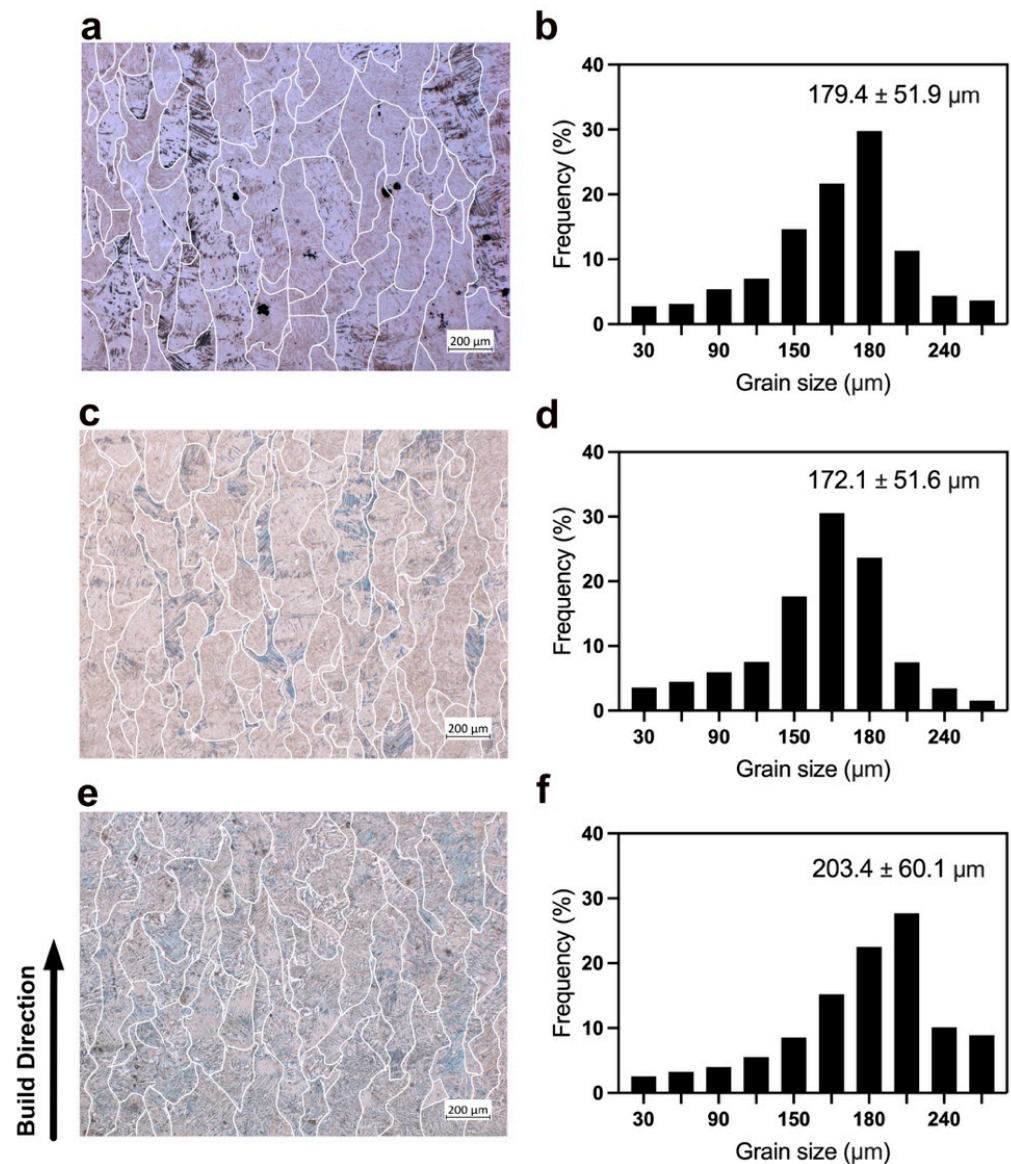


**Figure 6.** Representative optical microscopy images of (a) 950-WQ sample; (c) 950-AC sample; (e) 950-FC sample. The prior  $\beta$  grain boundaries in (a,c,e) are traced by white-color lines. The histograms of prior  $\beta$ -phase grains size are shown in (b,d,f).

### 3.2.2. $\alpha$ Microstructure Characterization with Different Heat Treatments

The microstructures of SLMed Ti-64 samples after 750 °C annealing consisted of fine  $\alpha$  lath and continuous GB- $\alpha$  (Figure 7), and  $\alpha'$  martensite could be observed in other images. It could be found that the influence of cooling rates is minimal at 750 °C, with the average thickness of  $\alpha$  lath similar for all three cooling rates, measured as  $0.56 \pm 0.13 \mu\text{m}$  after furnace cooling,  $0.58 \pm 0.09 \mu\text{m}$  after air cooling, and  $0.64 \pm 0.13 \mu\text{m}$  after water quenching. This consistent  $\alpha$  lath thickness was attributed to the relatively high  $\alpha$  fraction at 750 °C (87%), which inhibits the growth of  $\alpha$  lath [37]. Furthermore,  $\alpha$  colony formation could be identified in the SLMed Ti-64 after 750 °C annealing (Figure 7c,d). The measured average width of the  $\alpha$  colony was  $15.4 \mu\text{m} \pm 3.4$  in the 750-WQ sample,  $10.3 \pm 3.7 \mu\text{m}$  in the 750-AC sample, and  $16.5 \pm 2.9 \mu\text{m}$  in the 750-FC sample, respectively (Figure 7).

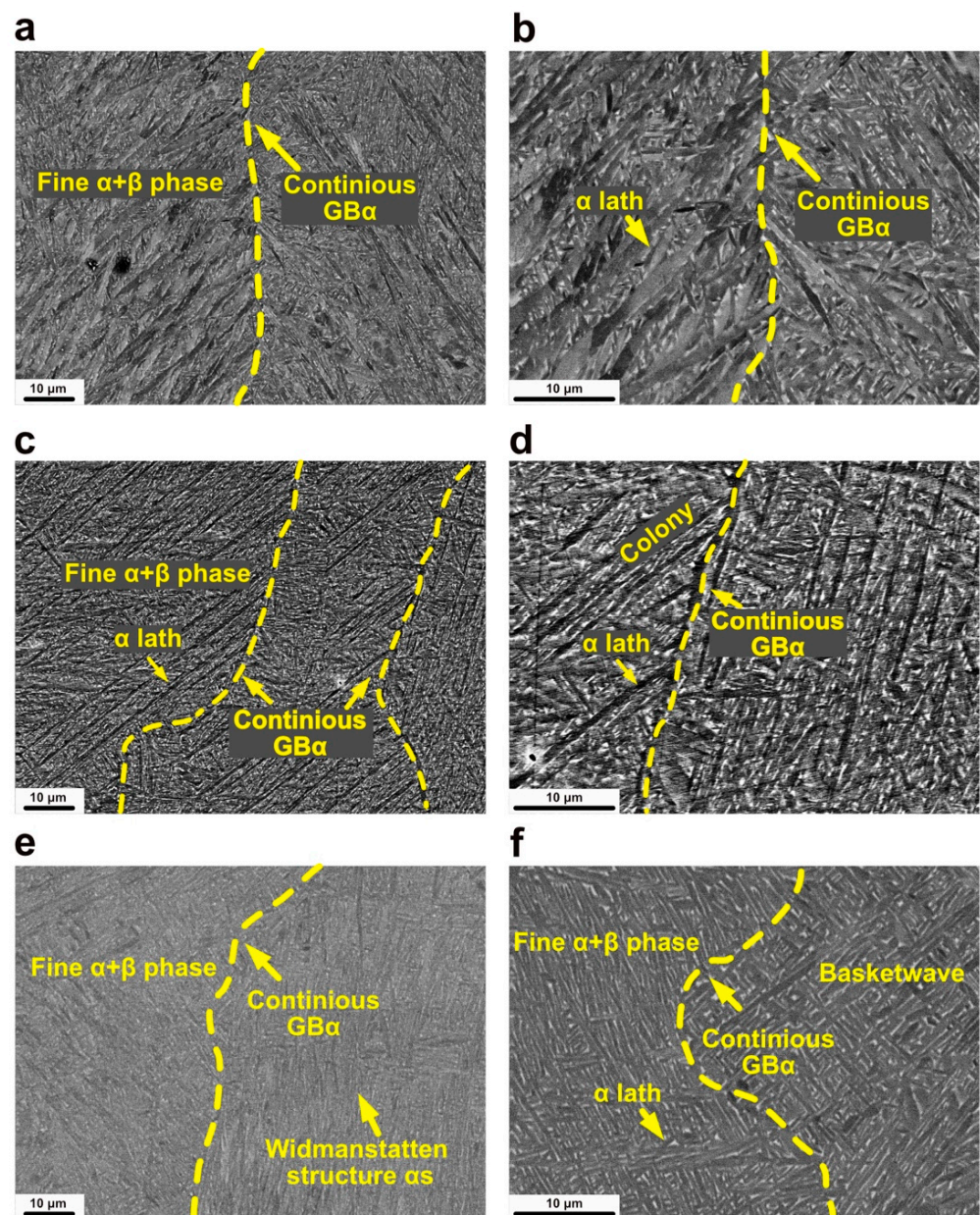


**Figure 7.** Microstructures in SLMed Ti64 with the different heat treatments, (a,b) 750-WQ, (c,d) 750-AC, (e,f) 750-FC.

After 850 °C annealing, the non-equilibrium  $\alpha'$  martensitic structure was further transformed to a mixture of  $\alpha$  and  $\beta$  phase, which was revealed as fine lath (Figure 8). By comparing with the  $\alpha$  lath in 750 °C annealed samples, those in 850 °C annealed samples became coarser, with the average thickness of  $\alpha$  lath  $0.71 \pm 0.17$ ,  $0.96 \pm 0.10$ , and  $1.15 \pm 0.14$   $\mu\text{m}$  in the 850-WQ sample, the 850-AC sample, and the 850-FC sample, respectively (Figure 8). Since the equilibrium  $\alpha$  fraction was still considerably high (73% at 850 °C), the influence of the cooling rate on the  $\alpha$  microstructure was not obvious [37]. This was attributed to the that the low-volume fraction of the  $\beta$  phase could not promote the growth of the  $\alpha$  phase. Furthermore, GB- $\alpha$  remained continuous after 850 °C annealing (Figure 8). The  $\alpha$  colonies around GB- $\alpha$  became coarser, with the width of  $\alpha$  colonies measured as  $28.2 \pm 5.1$   $\mu\text{m}$  after furnace cooling,  $28.1 \pm 4.8$   $\mu\text{m}$  after air cooling, and  $24.8 \pm 6.0$   $\mu\text{m}$  after water quenching (Figure 8).

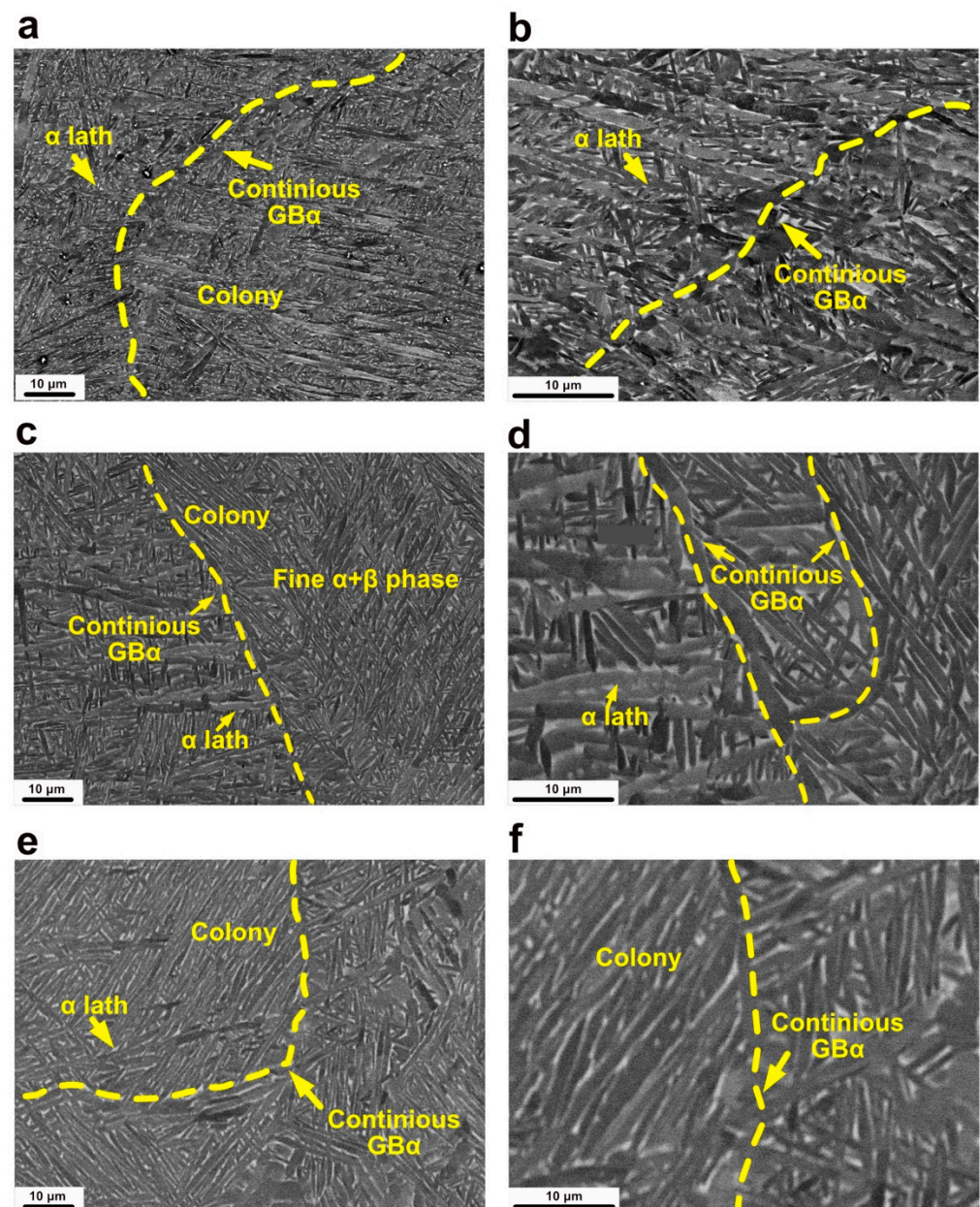


**Figure 8.** Microstructures in SLMed Ti64 with the different heat treatments, (a,b) 850-WQ, (c,d) 850-AC, (e,f) 850-FC.

With HT temperature close to the  $\beta$  transus, like 950 °C used in this study, the  $\alpha$  lath becomes coarser. This was attributed to the reduction of the equilibrium  $\alpha$  fraction to approximately 23% at 950 °C. During the cooling process, the high volume fraction of the  $\beta$  phase was favorable for the diffusion of  $\alpha$  stable elements and significantly promoted the growth of  $\alpha$  lath [37]. Furthermore, due to the lower amount of  $\alpha$  phase at 950 °C, the effect of cooling rate on the  $\alpha$  microstructure is profound, leading to the  $\alpha$  lath thickness of  $1.48 \pm 0.14 \mu\text{m}$  after water quenching,  $1.57 \pm 0.21 \mu\text{m}$  after air cooling and  $2.36 \pm 0.19 \mu\text{m}$  after furnace cooling (Figure 9). The samples after 950 °C annealing exhibited the discontinuous GB- $\alpha$  because the formation of  $\alpha$  lath broke the continuity of GB- $\alpha$  [38]. Furthermore, with smaller cooling rates, the presence of secondary  $\alpha$ -Widmanstatten structure could be identified (Figure 9c–f), which did not appear at the 750 °C/850 °C samples. During the cooling process, the formation of the  $\alpha$  phase is controlled by the solute atom diffusion, higher  $\beta$  volume fraction and the slow cooling rate are enough for the diffusion of the solution atoms. However, with the increased cooling rate, the diffusion of solution atoms

suppresses, which restrains the  $\alpha$ -grain growth [35,39]. Thus, secondary  $\alpha$ -Widmanstätten only appeared in samples with high HT temperature and low cooling rate.

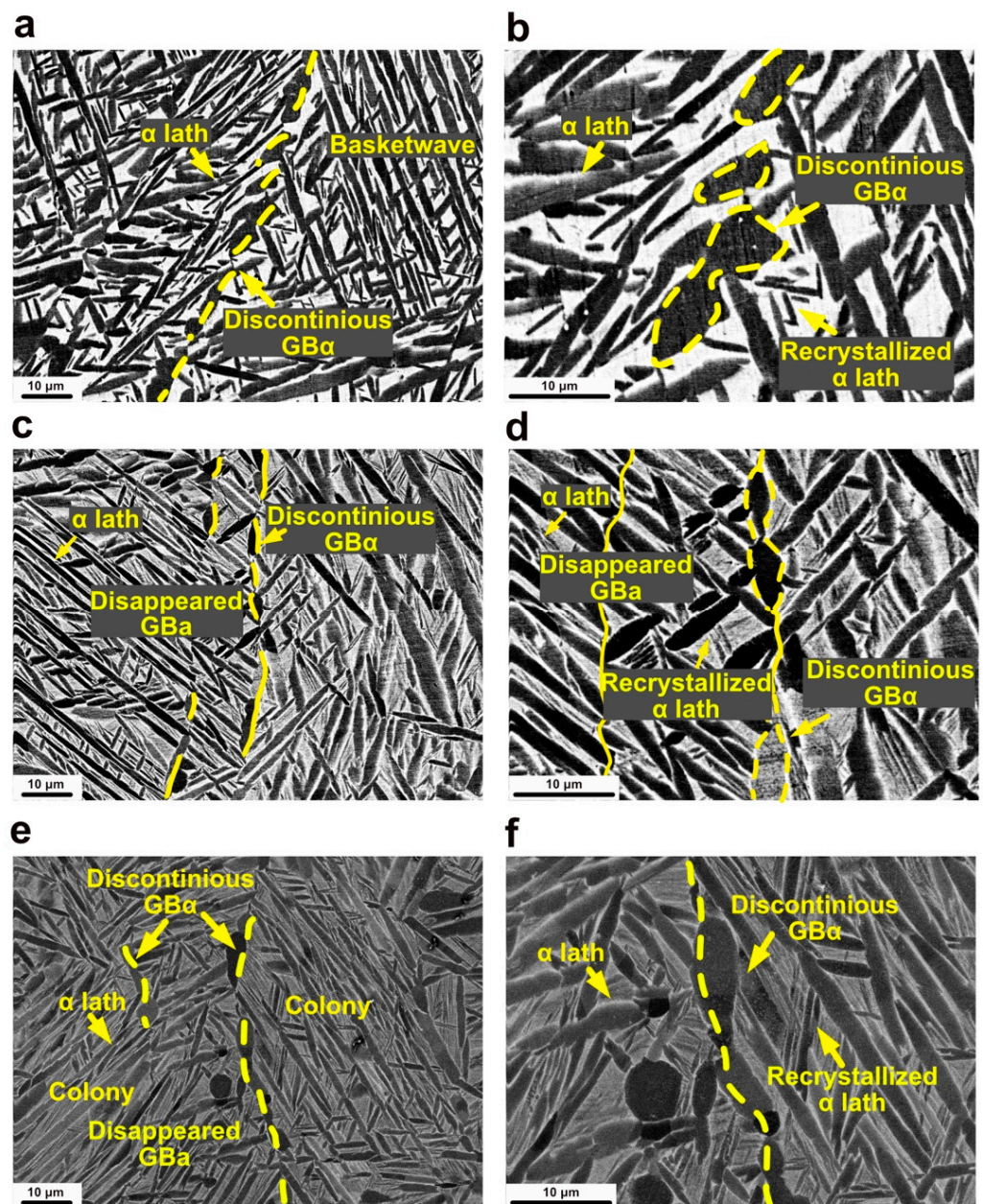


**Figure 9.** Microstructures in SLMed Ti64 with the different heat treatments, (a,b) 950-WQ, (c,d) 950-AC, (e,f) 950-FC.

### 3.3. Fracture Surface Characterization

The detailed fracture surface characterization of the 750-AC sample and the 850-AC sample after tensile failure shows evidence of the smooth fracture caused by continuous GB- $\alpha$  in the horizontal direction (denoted by the yellow circle in Figure 10a,c), even though the thickness of the GB- $\alpha$  was not consistently at the 750-AC sample and the 850-AC sample. The examination of the fracture surface in the vertical direction of the 750-AC sample and the 850-AC sample showed exhibited fine dimples, which confirmed the transgranular fracture (Figure 10b,d). The intergranular fracture indicates the low ductility in the horizontal direction of the 750-AC sample and the 850-AC sample, while the transgranular fracture indicates the high ductility in the vertical direction [40]. This shows the significant anisotropy in the 750-AC sample and the 850-AC samples, which

was consistent with a higher elongation for the vertical sample than that in the horizontal sample. For the 950-AC sample, both directions presented the intergranular fracture created by GB- $\alpha$  and the dimples caused by the transgranular fracture (Figure 10e–f). A similar fracture mode shows the 950-AC samples have a similar ductility in both directions, which also indicates the little tensile anisotropy at the 950-AC sample. These results show that the morphology of GB- $\alpha$  could influence the anisotropy of SLMed Ti-64.

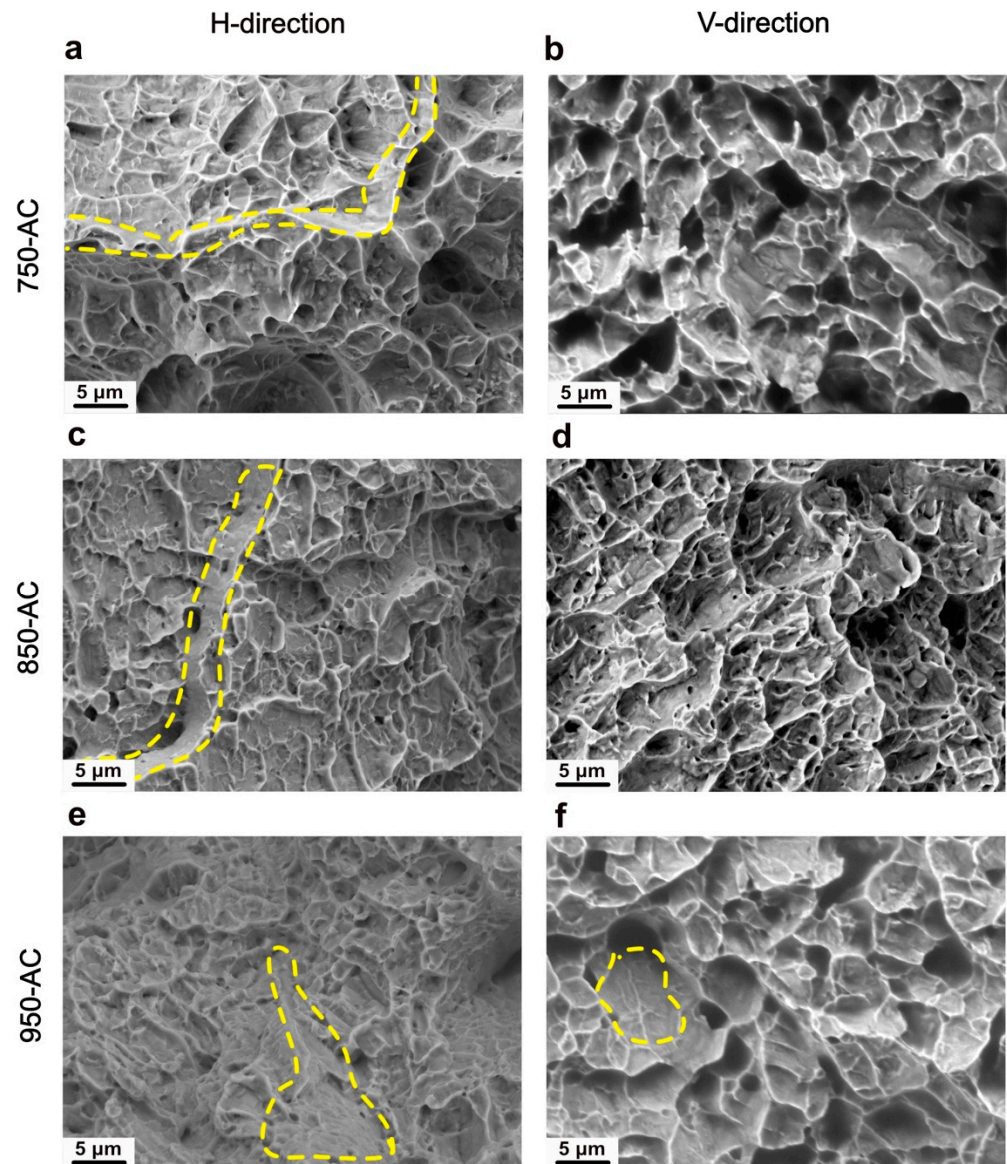


**Figure 10.** Fracture surface characterization of tensile failed samples by using secondary electron images: (a) 750-AC sample in the horizontal direction; (b) 750-AC sample in the vertical direction; (c) 850-AC sample in the horizontal direction; (d) 850-AC sample in the vertical direction; (e) 950-AC sample in the horizontal direction; (f) 950-AC sample in the vertical direction. Yellow circles are used to highlight the intergranular fracture caused by GB- $\alpha$ . The corresponding OM images of fracture surface could further distinguish fracture modes (Figure S1 in Supplementary Materials).

The further characterization of the longitudinal cross-section along the fracture surface showed that microstructure is the key to the tensile fracture behavior of SLMed Ti-64 in this study. In the horizontal sample of SLMed Ti-6Al-4V treated at 850 °C for 2 h, continuous grain boundary  $\alpha$  phase could be identified at the fracture surface (Figure 11a). Continuous GB- $\alpha$  was known to nucleate cracks and serve as a potential crack pathway under tensile loading [41,42]. Furthermore, the presence of continuous GB- $\alpha$  was correlated with the

columnar prior  $\beta$  grain, and the long axes of the prior  $\beta$  grain which were decorated with continuous GB- $\alpha$  phase are subjected to tension axis in the horizontal sample [19]. The prior  $\beta$  grain boundaries with continuous GB- $\alpha$  could be less resistant to the fracture and be easily delaminated during the tensile loading perpendicular to the long axes, which led to the intergranular fracture. This led to the lower ductility in the horizontal direction.

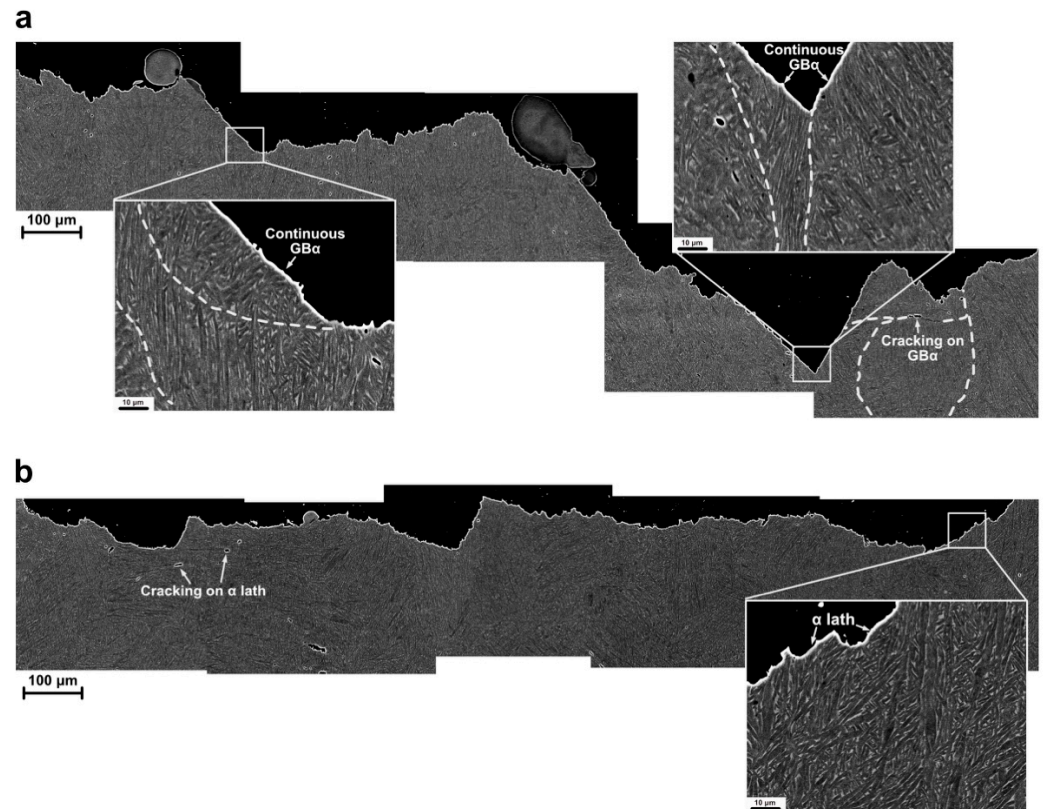


**Figure 11.** The fracture surface cross-section characterization of SLMed Ti-64 annealed at 850 °C in two directions: (a) horizontal direction; (b) vertical direction. The prior  $\beta$  grain boundaries were traced with white dot lines.

In the vertical sample of SLMed Ti-6Al-4V at 850 °C for 2 h, it could be found that cracks propagated around  $\alpha$  lath (Figure 11). In this case, it was found that tensile loads only act to the short axes part of prior  $\beta$  grain boundaries or GB- $\alpha$ , which made it difficult for the crack tip to propagate along the prior  $\beta$  grain boundaries [19]. With the cracks propagating within the prior  $\beta$  grains, the  $\alpha$  laths (like the ones in the 850-AC sample) increased the resistance of the crack propagation that led to the fracture at the  $\alpha$  lath interface. The examination of the fracture surface in the 850-AC sample shows the transgranular fracture, which also supports the above-mentioned discussion. Thus, the total elongation of the vertical sample was higher compared with that of the horizontal sample.

Due to the prior  $\beta$  grains with a low aspect ratio and the presence of discontinuous GB- $\alpha$  in SLMed Ti-64 annealed at 950 °C for 2 h, the fracture surface profiles along both directions are similar, indicating the consistent fracture modes (Figure 12). The fracture surface profiles of both direction samples manifest that cracks have propagated mainly along with  $\alpha$  lath. The prior  $\beta$  grain boundary, along with the decorated discontinuous GB- $\alpha$ , was not favored for the crack propagation in the 950-AC sample. This was attributed to that  $\alpha$  lath between discontinuous GB- $\alpha$  (Figure 9) inhibiting the crack propagation along the prior  $\beta$  grain boundaries, resulting in the transgranular failure in the 950-AC sample. Thus, the presence of discontinuous GB- $\alpha$  improved the elongation of the 950-AC samples, and the consistent fracture modes in both directions reduced the anisotropic ductility.

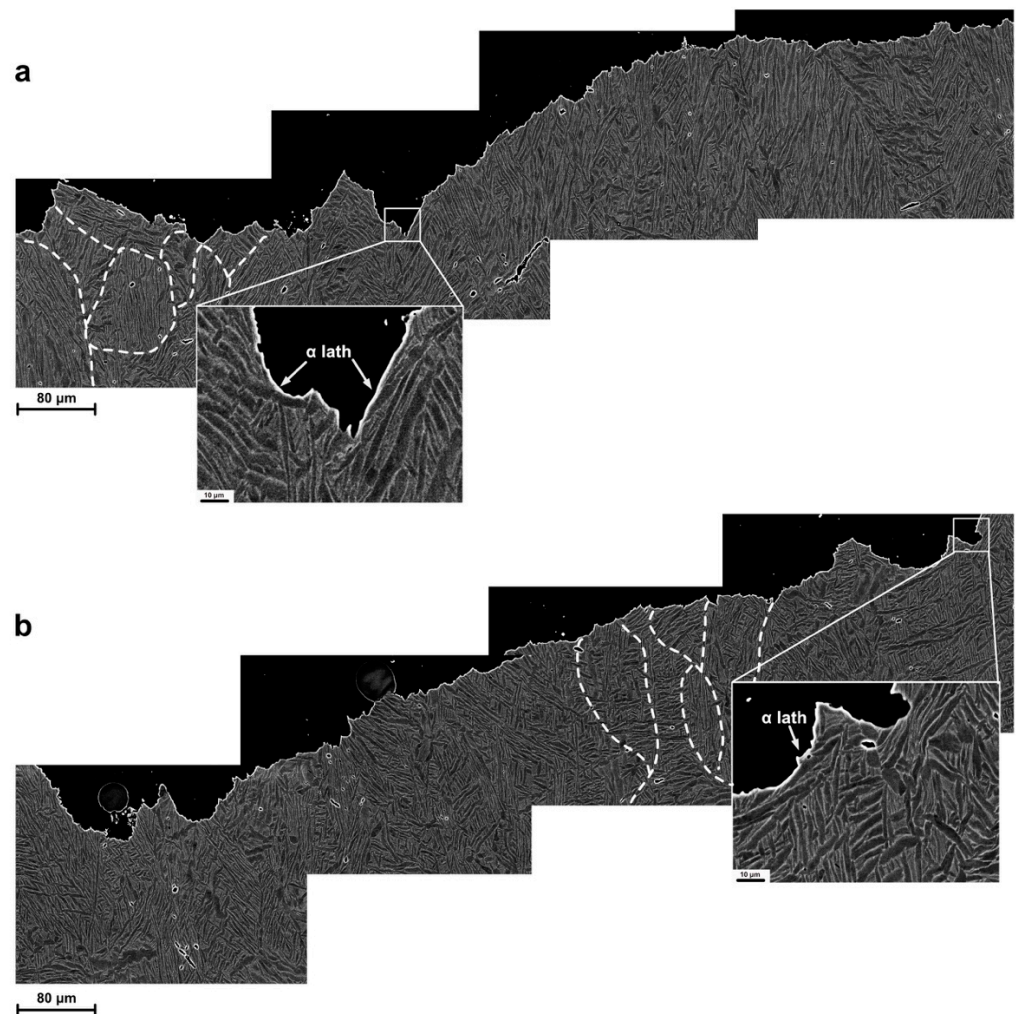


**Figure 12.** The fracture surface cross-section characterization of SLMed Ti-64 annealed at 950 °C in two directions: (a) horizontal direction; (b) vertical direction. The prior- $\beta$  grain boundaries were traced by white dot lines.

#### 4. Discussion

Numerous studies reported the mechanical property anisotropy in additive manufactured titanium alloys, with most of them showing the ductility measured in the vertical direction higher than that in the horizontal direction [43,44]. The microstructure heterogeneity, which includes the presence of large columnar grains, strong solidification texture, and continuous GB- $\alpha$ , is considered causing this mechanical property anisotropy. In AMed Ti-64, the columnar prior  $\beta$  grains have the long axes aligned with the fabrication direction and short axes perpendicular to the build direction, and the strain incompatibility between the columnar prior  $\beta$  grains could result in the crack preferentially initiating at grain boundaries [40,41,44]. Furthermore, the boundaries of the columnar prior  $\beta$  grains are decorated with GB- $\alpha$ . The presence of continuous GB- $\alpha$  was known to reduce the fracture resistance in conventionally manufactured Ti-6Al-4V by serving as the preferential pathway for crack propagation along prior  $\beta$  grain boundaries [45]. Thus, columnar prior  $\beta$  grains in AMed Ti-64 could lead to the different amounts of GB- $\alpha$  being exposed to the potential failure mode. In samples where tension is applied in the horizontal direction, the long axes of the prior  $\beta$  grain boundaries (and GB- $\alpha$ ) are loaded in tension. In contrast, when tension is applied in the vertical direction of the sample, only the short axes of the prior  $\beta$  grain boundaries (and GB- $\alpha$ ) are loaded in tension. However, discontinuous GB- $\alpha$  could directly hinder the crack propagation along the prior  $\beta$  grain boundaries and lead to both

the intercrystalline and transgranular fracture. The  $\alpha$  lath between the discontinuous GB- $\alpha$  could serve as a crack propagation inhibitor [31,46].

In this study, the presence of continuous GB- $\alpha$  led to the transgranular fracture, which results in the significant ductility difference between the vertical direction and the horizontal direction. Meanwhile, the discontinuous GB- $\alpha$  in the 950-AC sample led to the fracture mixed with the intercrystalline and transgranular modes and resulted in consistent ductility in both the vertical and horizontal directions. The strength difference in AMed titanium alloys caused by the crystallographic texture and the crystallographic orientation of  $\alpha$  lath, which is attributed to that crystallographic orientation can affect the deformation behavior of grains [42,47,48]. Furthermore, the different morphology of GB- $\alpha$  also affects the strength difference between the horizontal direction and vertical direction, because the presence of continuous GB- $\alpha$  leads to a significant reduction of fracture resistance, which decreases the tensile strength of the samples [22,49].

Whereas the above discussion considers the different morphology of GB- $\alpha$  resulting in different failure modes, a linear relationship between the discontinuous ratio of GB- $\alpha$  ( $x$ ) and the anisotropic ductility ( $y$ ) could be established [50,51], and was expressed by using Equation (1):

$$y = 0.25x + 0.81, \quad (1)$$

in which the discontinuous ratio of GB- $\alpha$  was defined by the number of segments with the GB- $\alpha$  less than 50  $\mu\text{m}$  divided by 500. As shown in Figure 13, with the discontinuous ratio of GB- $\alpha$  larger than 0.6 (like those in 750-AC, 750-FC, 850-AC, 850-FC, and 850-WQ), the ductility of SLMed Ti-64 becomes isotropic. The small discontinuous ratio of GB- $\alpha$  (like those in 950-AC and 950-FC) makes the ductility of SLMed Ti-64 anisotropic. This calculation further confirms that the elimination of continuous grain boundary  $\alpha$  phase is a promising approach that could eliminate the anisotropy ductility and provide significant guidance for the design of the heat treatment process. Furthermore, although the fracture mode for GB- $\alpha$  in Ti alloys has been proposed, the underlying mechanisms need some further investigation, which could help the mechanical property manipulation of other AM processed titanium alloys.

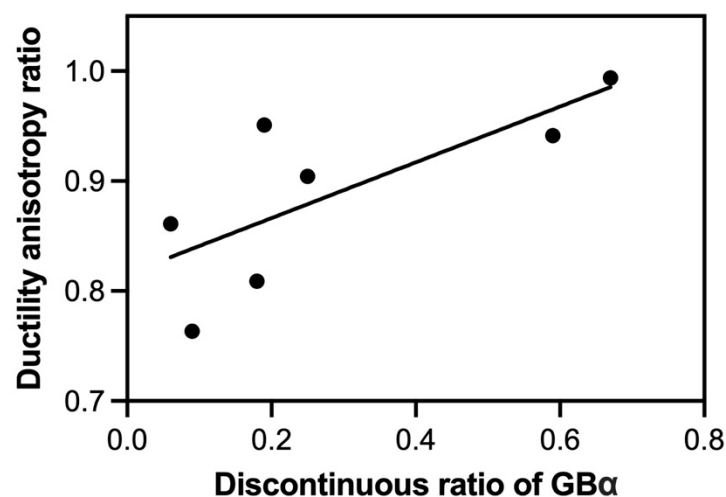


**Figure 13.** The relationship between the anisotropic ductility ratio (horizontal elongation/vertical elongation) and the discontinuous ratio of GB- $\alpha$ .

## 5. Conclusions

In this study, an investigation of the influence of different heat treatments on the microstructures, and the tensile performances of selective laser melted Ti-64 was carried out, with the effects of prior  $\beta$  grain and GB- $\alpha$  morphologies on tensile ductility correlated. The following conclusions can be drawn from this study:

1. The as-fabricated sample showed the columnar prior  $\beta$  grains. After sub-transus annealing, columnar prior  $\beta$  grains remain visible. With increased HT temperature, the width of prior  $\beta$  grains increased while the aspect ratio decreased. Additionally, the cooling rates had negligible influences on prior  $\beta$  grain growth.
2. As-fabricated Ti-64 showed the fully  $\alpha'$  martensite with the presence of GB- $\alpha$  hardly noticed at the prior  $\beta$  grain boundaries. With heat treatments used,  $\alpha'$  martensite could be decomposed into  $\alpha + \beta$  phase, along with the formation of GB- $\alpha$ . The thickness of the  $\alpha$  lath after sub-transus heat treatment (HT) is primarily dependent on the maximum HT temperature and the cooling rate. The morphology of GB- $\alpha$  is mainly dependent on the HT temperature, the GB- $\alpha$  exhibit the discontinuous morphology when HT temperatures increase to near the  $\beta$  transus (950 °C).
3. Tensile performances are very much dependent on HT temperature. With the increase of HT temperature, tensile strength declines and the total elongation rises because of acicular  $\alpha'$  martensite transformation to the coarser  $\alpha$  lath. However, the WQ samples present different trends, which is attributed to the fact that the high cooling rate leads to the high-temperature  $\beta$  phase being transformed to  $\alpha'$  martensite again.
4. The anisotropic ductility and the discontinuous ratio of GB- $\alpha$  could be correlated. With the discontinuous ratio of GB- $\alpha$  larger than 0.6, the anisotropic ductility of SLMed Ti-64 could be eliminated. The discontinuous GB- $\alpha$  results in the same failure mode in both directions which reduced their anisotropic ductility.

Furthermore, this study detailed studied the microstructural evolution of GB- $\alpha$ . To the best of our knowledge, this study first established the correlation between the discontinuous ratio of GB- $\alpha$  and anisotropic ductility in SLMed Ti-64. These findings may shed light on how to control post heat-treatment conditions to reduce the anisotropic ductility of SLMed Ti-64.

**Supplementary Materials:** The following are available online at <https://www.mdpi.com/article/10.3390/met11101593/s1>, Figure S1: Fracture surface characterization of tensile failed samples by using OM images: (a) 750-AC sample in the horizontal direction; (b) 750-AC sample in the vertical direction; (c) 850-AC sample in the horizontal direction; (d) 850-AC sample in the vertical direction; (e) 950-AC sample in the horizontal direction; (f) 950-AC sample in the vertical direction.

**Author Contributions:** Conceptualization, J.L. (Jianwen Liu) and K.Z.; methodology, J.L. (Jianwen Liu) and J.L. (Jie Liu); validation, J.L. (Jie Liu) and Y.L.; formal analysis, J.L. (Jianwen Liu), R.Z. and K.Z.; resources, R.Z., Z.Z., K.Z., Y.Z. and A.H.; writing—original draft preparation, J.L. (Jianwen Liu) and K.Z.; writing—review and editing, R.Z., Z.Z. and K.Z.; visualization, J.L. (Jianwen Liu), J.L. (Jie Liu) and Y.L.; supervision, K.Z.; funding acquisition, K.Z., Y.Z. and A.H. All authors have read and agreed to the published version of the manuscript.

**Funding:** This research was funded by Shanghai Municipal Education Commission, Sailing Program (grant number 20YF1431600), and the internal funding from University of Shanghai for Science and Technology.

**Institutional Review Board Statement:** Not applicable.

**Informed Consent Statement:** Not applicable.

**Data Availability Statement:** The data presented in this study are available on request from the corresponding author.

**Conflicts of Interest:** The authors declare no conflict of interest.

## References

1. Gu, D.; Shi, X.; Poprawe, R.; Bourell, D.L.; Rossitza Setchi, J.Z. Material-structure-performance integrated laser-metal additive manufacturing. *Science* **2021**, *372*. [[CrossRef](#)]
2. DebRoy, T.; Wei, H.L.; Zuback, J.S.; Mukherjee, T.; Elmer, J.W.; Milewski, J.O.; Beese, A.M.; Wilson-Heid, A.; De, A.; Zhang, W. Additive manufacturing of metallic components—Process, structure and properties. *Prog. Mater. Sci.* **2018**, *92*, 112–224. [[CrossRef](#)]
3. Herzog, D.; Seyda, V.; Wycisk, E.; Emmelmann, C. Additive manufacturing of metals. *Acta Mater.* **2016**, *117*, 371–392. [[CrossRef](#)]

4. Gibbons, D.W.; Serfontein, J.P.L.; van der Merwe, A.F. Mapping the path to certification of metal laser powder bed fusion for aerospace applications. *Rapid Prototyp. J.* **2021**, *27*, 355–361. [[CrossRef](#)]
5. Sanaei, N.; Fatemi, A. Defects in additive manufactured metals and their effect on fatigue performance: A state-of-the-art review. *Prog. Mater. Sci.* **2020**, *117*, 100724. [[CrossRef](#)]
6. Foehring, D.; Chew, H.B.; Lambros, J. Characterizing the tensile behavior of additively manufactured Ti-6Al-4V using multiscale digital image correlation. *Mater. Sci. Eng. A* **2018**, *724*, 536–546. [[CrossRef](#)]
7. Gong, H.; Rafi, K.; Gu, H.; Janaki Ram, G.D.; Starr, T.; Stucker, B. Influence of defects on mechanical properties of Ti-6Al-4V components produced by selective laser melting and electron beam melting. *Mater. Des.* **2015**, *86*, 545–554. [[CrossRef](#)]
8. Zhang, R.; Liu, Z.; Huang, J.; Zhu, Q.; Xiao, Z. Effect of Heat Treatment on Microstructure and Mechanical Properties of Inconel 718 Alloy Fabricated by Selective Laser Melting. *Rare Met. Mater. Eng.* **2021**, *50*, 255–262.
9. Murray, S.P.; Pusch, K.M.; Polonsky, A.T.; Torbet, C.J.; Seward, G.G.E.; Zhou, N.; Forsik, S.A.J.; Nandwana, P.; Kirka, M.M.; Dehoff, R.R.; et al. A defect-resistant Co–Ni superalloy for 3D printing. *Nat. Commun.* **2020**, *11*, 1–11. [[CrossRef](#)]
10. Chen, W.; Voisin, T.; Zhang, Y.; Florien, J.B.; Spadaccini, C.M.; McDowell, D.L.; Zhu, T.; Wang, Y.M. Microscale residual stresses in additively manufactured stainless steel. *Nat. Commun.* **2019**, *10*, 1–12. [[CrossRef](#)]
11. Wang, Y.M.; Voisin, T.; McKeown, J.T.; Ye, J.; Calta, N.P.; Li, Z.; Zeng, Z.; Zhang, Y.; Chen, W.; Roehling, T.T.; et al. Additively manufactured hierarchical stainless steels with high strength and ductility. *Nat. Mater.* **2018**, *17*, 63–70. [[CrossRef](#)]
12. Zhang, B.; Han, X.; Chen, C.; Zhang, W.; Liao, H.; Chen, B. Effect of the strut size and tilt angle on the geometric characteristics of selective laser melting AlSi10Mg. *Rapid Prototyp. J.* **2021**, *27*, 879–889. [[CrossRef](#)]
13. Guan, J.; Wang, Q.; Chen, C.; Xiao, J. Forming feasibility and interface microstructure of Al/Cu bimetallic structure fabricated by laser powder bed fusion. *Rapid Prototyp. J.* **2021**, *27*, 1337–1345. [[CrossRef](#)]
14. González, J.E.; de Armas, G.; Negrin, J.; Beltrán, A.M.; Trueba, P.; Gotor, F.J.; Peón, E.; Torres, Y. Influence of successive chemical and thermochemical treatments on surface features of Ti6Al4V samples manufactured by SLM. *Metals* **2021**, *11*, 313. [[CrossRef](#)]
15. Fan, W.; Tan, H.; Zhang, F.; Feng, Z.; Wang, Y.; Zhang, L.-C.; Lin, X.; Huang, W. Overcoming the limitation of in-situ microstructural control in laser additive manufactured Ti-6Al-4V alloy to enhanced mechanical performance by integration of synchronous induction heating. *J. Mater. Sci. Technol.* **2021**, *94*, 32–46. [[CrossRef](#)]
16. Lütjering, G.; Williams, J.C. *Titanium*; Springer: New York, NY, USA, 2003.
17. Birmingham, M.J.; StJohn, D.H.; Krynen, J.; Tedman-Jones, S.; Dargusch, M.S. Promoting the columnar to equiaxed transition and grain refinement of titanium alloys during additive manufacturing. *Acta Mater.* **2019**, *168*, 261–274. [[CrossRef](#)]
18. Yang, K.V.; Shi, Y.; Palm, F.; Wu, X.; Rometsch, P. Columnar to equiaxed transition in Al-Mg(-Sc)-Zr alloys produced by selective laser melting. *Scr. Mater.* **2018**, *145*, 113–117. [[CrossRef](#)]
19. Carroll, B.E.; Palmer, T.A.; Beese, A.M. Anisotropic tensile behavior of Ti-6Al-4V components fabricated with directed energy deposition additive manufacturing. *Acta Mater.* **2015**, *87*, 309–320. [[CrossRef](#)]
20. Birmingham, M.J.; McDonald, S.D.; Dargusch, M.S.; StJohn, D.H. The mechanism of grain refinement of titanium by silicon. *Scr. Mater.* **2008**, *58*, 1050–1053. [[CrossRef](#)]
21. Zhang, D.; Qiu, D.; Gibson, M.A.; Zheng, Y.; Fraser, H.L.; StJohn, D.H.; Easton, M.A. Additive manufacturing of ultrafine-grained high-strength titanium alloys. *Nature* **2019**, *576*, 91–95. [[CrossRef](#)]
22. Birmingham, M.J.; McDonald, S.D.; Dargusch, M.S. Effect of trace lanthanum hexaboride and boron additions on microstructure, tensile properties and anisotropy of Ti-6Al-4V produced by additive manufacturing. *Mater. Sci. Eng. A* **2018**, *719*, 1–11. [[CrossRef](#)]
23. Zhang, K.; Tian, X.; Birmingham, M.; Rao, J.; Jia, Q.; Zhu, Y.; Wu, X.; Cao, S.; Huang, A. Effects of boron addition on microstructures and mechanical properties of Ti-6Al-4V manufactured by direct laser deposition. *Mater. Des.* **2019**, *184*, 108191. [[CrossRef](#)]
24. Vrancken, B.; Thijs, L.; Kruth, J.P.; Van Humbeeck, J. Heat treatment of Ti6Al4V produced by Selective Laser Melting: Microstructure and mechanical properties. *J. Alloy. Compd.* **2012**, *541*, 177–185. [[CrossRef](#)]
25. Cao, S.; Chu, R.; Zhou, X.; Yang, K.; Jia, Q.; Lim, C.V.S.; Huang, A.; Wu, X. Role of martensite decomposition in tensile properties of selective laser melted Ti-6Al-4V. *J. Alloy. Compd.* **2018**, *744*, 357–363. [[CrossRef](#)]
26. Deng, H.; Qiu, W.; Cao, S.; Chen, L.; Hu, Z.; Wei, Y.; Xia, Z.; Zhou, L.; Cui, X.; Tang, J. Heat-treatment induced microstructural evolution and enhanced mechanical property of selective laser melted near  $\beta$  Ti-5Al-5Mo-5 V-3Cr-1Zr alloy. *J. Alloy. Compd.* **2021**, *858*, 158351. [[CrossRef](#)]
27. Zhao, Z.; Chen, J.; Tan, H.; Zhang, G.; Lin, X.; Huang, W. Achieving superior ductility for laser solid formed extra low interstitial Ti-6Al-4V titanium alloy through equiaxial alpha microstructure. *Scr. Mater.* **2018**, *146*, 187–191. [[CrossRef](#)]
28. Jiang, X.J.; Zhao, H.T.; Yu, G.; Wu, H.Y.; Tan, C.L.; Zhang, X.Y.; Ma, M.Z.; Liu, R.P. Structural evolution and mechanical properties of Ti-41Zr-7.3Al alloy during continuous cooling process. *J. Alloy. Compd.* **2017**, *725*, 750–756. [[CrossRef](#)]
29. Liu, C.; Lu, Y.; Tian, X.; Liu, D. Influence of continuous grain boundary  $\alpha$  on ductility of laser melting deposited titanium alloys. *Mater. Sci. Eng. A* **2016**, *661*, 145–151. [[CrossRef](#)]
30. Osovski, S.; Srivastava, A.; Williams, J.C.; Needleman, A. Grain boundary crack growth in metastable titanium  $\beta$  alloys. *Acta Mater.* **2015**, *82*, 167–178. [[CrossRef](#)]
31. Liu, C.M.; Wang, H.M.; Tian, X.J.; Liu, D. Development of a pre-heat treatment for obtaining discontinuous grain boundary  $\alpha$  in laser melting deposited Ti-5Al-5Mo-5V-1Cr-1Fe alloy. *Mater. Sci. Eng. A* **2014**, *604*, 176–182. [[CrossRef](#)]

32. Chen, Z.; Wu, X.; Tomus, D.; Davies, C.H.J. Surface roughness of Selective Laser Melted Ti-6Al-4V alloy components. *Addit. Manuf.* **2018**, *21*, 91–103. [[CrossRef](#)]
33. Chen, Z.; Wu, X.; Davies, C.H.J. Process variation in Laser Powder Bed Fusion of Ti-6Al-4V. *Addit. Manuf.* **2021**, *41*, 101987. [[CrossRef](#)]
34. Zhao, Z.; Chen, J.; Lu, X.; Tan, H.; Lin, X.; Huang, W. Formation mechanism of the  $\alpha$  variant and its influence on the tensile properties of laser solid formed Ti-6Al-4V titanium alloy. *Mater. Sci. Eng. A* **2017**, *691*, 16–24. [[CrossRef](#)]
35. Xu, J.; Zeng, W.; Zhao, Y.; Sun, X.; Du, Z. Influence of cooling rate following heat treatment on microstructure and phase transformation for a two-phase alloy. *J. Alloy. Compd.* **2016**, *688*, 301–309. [[CrossRef](#)]
36. Liu, F.; He, C.; Chen, Y.; Zhang, H.; Wang, Q.; Liu, Y. Effects of defects on tensile and fatigue behaviors of selective laser melted titanium alloy in very high cycle regime. *Int. J. Fatigue* **2020**, *140*, 105795. [[CrossRef](#)]
37. Pederson, R.; Babushkin, O.; Skystedt, F.; Warren, R. Use of high temperature X-ray diffractometry to study phase transitions and thermal expansion properties in Ti-6Al-4V. *Mater. Sci. Technol.* **2003**, *19*, 1533–1538. [[CrossRef](#)]
38. Zhang, Y.; Xin, R.; Guo, B.; Wang, K.; Liu, Q. Influence of alternate grain boundary  $\alpha$  on the development of Widmanstätten microstructure in TC21 Ti alloy. *Mater. Charact.* **2021**, *177*, 111162. [[CrossRef](#)]
39. Shao, H.; Zhao, Y.; Ge, P.; Zeng, W. Influence of Cooling Rate and Aging on the Lamellar Microstructure and Fractography of TC21 Titanium Alloy. *Metallogr. Microstruct. Anal.* **2013**, *2*, 35–41. [[CrossRef](#)]
40. Wilson-Heid, A.E.; Wang, Z.; McCornac, B.; Beese, A.M. Quantitative relationship between anisotropic strain to failure and grain morphology in additively manufactured Ti-6Al-4V. *Mater. Sci. Eng. A* **2017**, *706*, 287–294. [[CrossRef](#)]
41. Xu, Z.W.; Liu, A.; Wang, X.S. The influence of building direction on the fatigue crack propagation behavior of Ti6Al4V alloy produced by selective laser melting. *Mater. Sci. Eng. A* **2019**, *767*, 138409. [[CrossRef](#)]
42. Tian, X.; Zhu, Y.; Lim, C.V.S.; Williams, J.; Boyer, R.; Wu, X.; Zhang, K.; Huang, A. Isotropic and Improved Tensile Properties of Ti-6Al-4V Achieved by In-situ Rolling in Direct Energy Deposition. *Addit. Manuf.* **2021**, *46*, 102151. [[CrossRef](#)]
43. Sun, W.; Ma, Y.; Huang, W.; Zhang, W.; Qian, X. Effects of build direction on tensile and fatigue performance of selective laser melting Ti6Al4V titanium alloy. *Int. J. Fatigue* **2020**, *130*, 105260. [[CrossRef](#)]
44. Simonelli, M.; Tse, Y.Y.; Tuck, C. Effect of the build orientation on the mechanical properties and fracture modes of SLM Ti-6Al-4V. *Mater. Sci. Eng. A* **2014**, *616*, 1–11. [[CrossRef](#)]
45. Eylon, D. Fatigue crack initiation in hot isostatically pressed Ti-6Al-4V castings. *J. Mater. Sci.* **1979**, *14*, 1914–1922. [[CrossRef](#)]
46. Xie, Y.; Gong, M.; Luo, Z.; Li, Q.; Gao, M.; Wang, F.; Zeng, X.; Wang, G. Effect of microstructure on short fatigue crack growth of wire arc additive manufactured Ti-6Al-4V. *Mater. Charact.* **2021**, *177*, 111183. [[CrossRef](#)]
47. Liu, J.; Zhang, K.; Yang, Y.; Wang, H.; Zhu, Y.; Huang, A. Grain boundary  $\alpha$ -phase precipitation and coarsening: Comparing laser powder bed fusion with as-cast Ti-6Al-4V. *Scr. Mater.* **2022**, *207*, 114261. [[CrossRef](#)]
48. Liu, Z.; Zhao, Z.B.; Liu, J.; Wang, Q.; Guo, Z.; Zeng, Y.; Yang, G.; Gong, S. Effects of the crystallographic and spatial orientation of  $\alpha$  lamellae on the anisotropic in-situ tensile behaviors of additive manufactured Ti-6Al-4V. *J. Alloy. Compd.* **2021**, *850*, 156886. [[CrossRef](#)]
49. Mine, Y.; Matsuzaki, Y.; Takashima, K. Anisotropy of strength and plasticity in single-colony lamellar structure of Ti-6Al-4V alloy. *Scr. Mater.* **2020**, *177*, 223–228. [[CrossRef](#)]
50. Xie, Y.; Gong, M.; Zhang, R.; Gao, M.; Zeng, X.; Wang, F. Grain boundary discontinuity and performance improvement mechanism of wire arc additive manufactured Ti-6Al-4V. *J. Alloy. Compd.* **2021**, *869*, 159287. [[CrossRef](#)]
51. Martina, F.; Colegrove, P.A.; Williams, S.W.; Meyer, J. Microstructure of Interpass Rolled Wire + Arc Additive Manufacturing Ti-6Al-4V Components. *Metall. Mater. Trans. A* **2015**, *46*, 6103–6118. [[CrossRef](#)]